



# Various facets of intermolecular transfer of phase coherence by nuclear dipolar fields

Philippe Pelupessy<sup>1</sup>

<sup>1</sup>Laboratoire des Biomolécules, LBM, Département de Chimie, École Normale Supérieure, PSL University, Sorbonne Université, CNRS, 75005 Paris, France

**Correspondence:** Philippe Pelupessy (philippe.pelupessy@ens.psl.eu)

**Abstract.** Several pulse sequences that allow for an intermolecular transfer of phase coherence from abundant solvent to sparse solute spins are presented. The transfer is mediated by dipolar fields stemming from the solvent nuclei and occurs during suitable uninterrupted radio-frequency pulse-trains. Theoretical expressions for the evolution of the solvent magnetization under continuous irradiation are derived. A pulse sequence for the retrieval of high-resolution spectra in inhomogeneous magnetic fields is described, and another sequence to detect a double quantum transfer. In addition, various schemes where the magnetization is modulated with multiple pulsed field gradients along different directions are discussed. **In these schemes, the dipolar field can be decomposed into two components, each at the helm of its own transfer.**

## 1 Introduction

In liquid state NMR, the magnetization of an abundant or a highly polarized spin species affects the evolution of the density operator through radiation damping (RD) (Suryan, 1949) and through the dipolar field (DF) (Dickinson, 1951). RD stems from the radio-frequency (rf) field caused by the current that the transverse magnetization induces in an rf coil (Bloembergen and Pound, 1954). The DF describes the direct contributions of the longitudinal and transverse nuclear magnetization components to the static field  $B_0$  and a perpendicular rf field  $B_1$ , respectively, through dipolar interactions. Both phenomena can be incorporated into a modified set of Bloch equations (Bloom, 1957; Deville et al., 1979). The effects of RD on other resonances is usually limited to nearby frequencies, since RD results in a field with only a rapid oscillating transverse component. When the chemical shift differences are removed from the effective Hamiltonian by suitable pulse sequences, the effects of RD extend over a much wider range of frequencies (Pelupessy, 2022a). Conversely, the DF has a longitudinal component which causes a shift in the precession frequencies of all nuclei that possess a spin (Edzes, 1990). Striking effects are observed when the magnetization of abundant spin species depends on its position, often as a result of a pulsed field gradient (PFG). These non-trivial effects include multiple spin echoes in two-pulse experiments (Bernier and Delrieu, 1977; Bowtell et al., 1990) and intermolecular multiple quantum cross-peaks in correlation spectroscopy (COSY) like sequences. These peaks can stem from *like* (He et al., 1993) or *unlike* (Warren et al., 1993) spins. The phase-coherence of abundant spins can also be transferred by the DF during pulse-trains that are commonly used in homo-nuclear total correlation spectroscopy (TOCSY) (Pelupessy, 2022b). As with RD in these type of experiments, the small transverse component of the DF plays an important role even if



25 chemical shift differences are large. In this work, several aspects of this transfer will be elaborated upon: broadband in-phase  
transfer and high-resolution spectra can be obtained in inhomogeneous  $B_0$  fields in a fashion similar to the HOMOGENIZED  
(homogeneity enhancement by intermolecular zero-quantum detection, Vathyam et al. (1996)) and related experiments (Lin  
et al., 2013). In addition, a transfer of phase coherence can be realized from intermolecular double quantum (DQ) coherences  
involving the abundant solvent and the sparse solute spins. Finally, experiments where the magnetization is modulated in more  
30 complex ways by applying several PFGs in combination with selective rf pulses will be discussed.

## 2 Theory

The following theory applies to a homonuclear spin system that contains an abundant spin species  $A$  and a sparse spin species  
 $S$ . If the magnetization of the spins  $A$  is modulated in a manner that it averages out over the effective sample volume (Warren  
et al., 1995) by a PFG which is oriented at an angle  $\theta_G$  with respect to  $B_0$ , the amplitude of the DF can be defined as:

$$35 \quad \omega_D = \frac{1}{3} \mu_0 \gamma M_{eq}^A (3 \cos^2 \theta_G - 1), \quad (1)$$

with  $\gamma$  the gyro-magnetic ratio of the  $A$  and  $S$  spins,  $\mu_0$  the vacuum permeability, and  $M_{eq}^A$  the magnitude of the magnetization  
of the  $A$  spins at equilibrium. In the rotating frame, the evolution of the magnetization vectors of both  $A$  and  $S$  spins is governed  
by the modified Bloch equations (Deville et al., 1979; Bowtell et al., 1990; Enss et al., 1999):

$$\begin{aligned} \dot{m}_x^i &= -(\omega_0^i + \omega_D m_z^A) m_y^i + (\omega_{1y} - \omega_D m_y^A / 2) m_z^i, \\ \dot{m}_y^i &= (\omega_0^i + \omega_D m_z^A) m_x^i - (\omega_{1x} - \omega_D m_x^A / 2) m_z^i, \\ \dot{m}_z^i &= -(\omega_{1y} - \omega_D m_y^A / 2) m_x^i + (\omega_{1x} - \omega_D m_x^A / 2) m_y^i, \end{aligned} \quad (2)$$

40 with  $i$  either  $A$  or  $S$ ,  $\omega_{1x/y}$  the (time-dependent) rf field, and  $\omega_0$  the offset from the carrier frequency. The magnetization  
components, written in lower case  $m$ , are normalized with respect to the equilibrium amplitudes. These equations are local so  
that the evolution can be calculated separately for each position in the sample (Deville et al., 1979). The explicit position and  
time dependence of the variables has been omitted in these equations. A set time  $t = T$  will be indicated in brackets. Neither  
relaxation nor molecular motions by diffusion or convection have been taken into account.

45 The set of coupled eqs. 2 is non-linear when  $i = A$ , while for the sparse spins  $i = S$  the magnetization of the  $A$  spins  
 $\mathbf{m}^A$  is the source of a time-dependent field  $(-\omega_D m_x^A / 2, -\omega_D m_y^A / 2, \omega_D m_z^A)$ . Hence, the evolution of the magnetization of  
the  $S$  spins  $\mathbf{m}^S$  can be calculated straightforwardly from the trajectory of  $\mathbf{m}^A$ . For a strong constant on-resonance rf field  
( $|\omega_1| \gg |\omega_D|$ ) along the  $x$ -axis,  $\mathbf{m}^A$  rotates around  $x$  with an angular frequency of  $\omega_{1x} - 3m_x^A(0)\omega_D/4$  (see appendix A).

Many sequences used for decoupling or magnetization transfer consist of a repetitive cycle of phase-alternated pulses along  
50 one axis (in this work, assumed between  $+x$  and  $-x$ ), as for example DIPSI-2 (decoupling in presence of scalar interactions,  
Rucker and Shaka (1989)), Waltz-16 (Shaka et al., 1983) and GARP (globally optimized alternating-phase rectangular pulses,  
Shaka et al. (1985)). Typically, the pulses are constant in amplitude, but may differ in duration. By design, the integral of the  
rf field  $\int \omega_{1x} dt$  averages to zero over one cycle. Consequently, the contribution of  $\omega_{1x}$  vanishes after each full cycle if eqs.



A6 govern the evolution during all pulses in the cycle. In fig. 1a-c, the validity of this approximation is tested for DIPSPI-2 by comparing the trajectories predicted by eqs. A6 with exact numerical simulations. When the initial magnetization is oriented far away from the  $x$ -axis the trajectories diverge at longer irradiation times  $t_p$  of the DIPSPI-2 pulse-train. These differences are due to the rapid switching of rf phases which results in small – but in the long run non-negligible – contributions of the rotating terms in eqs. A5. For shorter times  $t_p < 0.4$  s, the curves obtained by both methods agree quite well. For a continuous rf field, the curves calculated with the two methods are undistinguishable, while for a GARP pulse-train, where the phases are alternated 2.5 times more frequently than for DIPSPI-2 with the same rf amplitude, the deviations are much larger (see supporting information). Although one might be tempted to attribute this result to the higher phase switching rate, the details of the sequence are also important. For example, the use of WALTZ-16, with a phase switching rate that is 1.6 times more frequent than for DIPSPI-2, results in a perfect match between the trajectories calculated with the two methods. The elementary block of WALTZ-16 consists of three pulses  $90_x 180_{-x} 270_x$ , i.e. a  $180^\circ$  pulse flanked by two pulses whose sum is  $360^\circ$ . These angles make the oscillating terms in eqs. A5 run over exactly 1 and 2 full rotations.

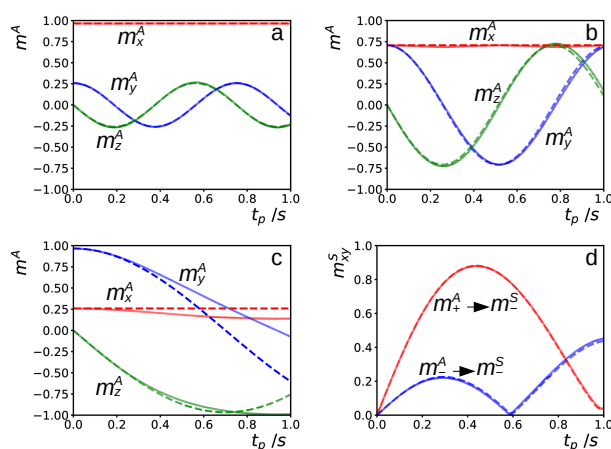


**Figure 1.** (a-c) Simulations of the evolution of the magnetization of the abundant spins  $A$ , during a time  $t_p$  of an on-resonance DIPSPI-2 pulse-train, for different initial conditions corresponding to magnetization in the  $xy$ -plane at angles of  $15^\circ$  (a),  $45^\circ$  (b) and  $75^\circ$  (c) with respect to the  $x$ -axis. The amplitude of the rf field was  $\nu_1 = 8.33$  kHz and of the DF  $\omega_D = 2\pi \times 1.84$  rad  $s^{-1}$ . The magnetization is recorded stroboscopically after each full cycle. The solid lines result from numerical integration of the modified Bloch equations 2 as in Pelupessy (2022b). The dashed lines correspond to eqs. A6 with  $\omega_{1x} = 0$ . (d) Simulation of the transfer of phase coherence from spins  $A$  to  $S$  with the experiment described in Pelupessy (2022b): a selective excitation of the  $A$  spins followed by a DIPSPI-2 pulse-train bracketed by two PFGs of equal area which have either equal (to observe a transfer  $m_+^A \rightarrow m_-^S$ ) or opposite signs ( $m_-^A \rightarrow m_+^S$ ). Similarly to (a-c), the trajectory of the magnetization of the  $A$  spins for each position has been obtained either by numerical integration (solid lines) or by neglecting the DF within each DIPSPI-2 cycle while using the approximate solution of eqs. A6 for the global evolution between the cycles (dashed lines).

65

Fig. 1d shows simulations of the intermolecular transfer of phase coherence due to the DF from spins  $A$  to spins  $S$  for a gradient-selected selective TOCSY experiment (Pelupessy, 2022b). As in fig. 1a-c, the solid lines have been obtained with the



trajectory of  $\mathbf{m}^A$  calculated by numerical integration of the non-linear coupled differential eqs. 2 as described in Pelupessy (2022a), while dashed lines with the trajectory predicted by eqs. A6. For the latter simulations, eqs. A6 with  $\omega_{1x} = 0$  have been used to calculate the evolution of  $\mathbf{m}^A$  between the DIPSI-2 cycles, while within each cycle the trajectory was assumed to be solely determined by the rf field. The dashed lines that can be calculated very rapidly are barely distinguishable from the solid ones that require more laborious simulations.

### 3 Experiments

In this section, several TOCSY-like experiments, where the DF mediates intermolecular transfer of phase coherence, will be discussed. While the above theory will be used to simulate the transfer, the formalism developed by Warren and coworkers (Lee et al., 1996) will be employed to guide the experimental design. For this, the high temperature approximation needs to be abandoned by taking into account higher order terms in the expansion of the density matrix:

$$\rho_{eq} = (\mathbb{1} - S_z) \prod_i (\mathbb{1} - A_{zi}) . \quad (3)$$

Since intermolecular interactions between sparse spins  $S$  can be neglected, the index  $i$  runs over all abundant spins  $A$ . In the experiments explored in this work, the equilibrium density operator evolves during a preparation period – before the DIPSI-2 irradiation – under the influence of rf pulses and PFGs. In this period, the DF will be neglected either because of its brevity or because the relevant part of the density operator commutes with the effective dipolar Hamiltonian. The intermolecular dipolar interactions between the  $A$  and  $S$  spins need to be tracked. The effective intermolecular dipolar Hamiltonian during the DIPSI-2 sequence is given by (Kramer et al., 2001):

$$H_{AS}^{eff} = -A_x S_x + (A_y S_y + A_z S_z)/2 . \quad (4)$$

The transfer induced by the DF can be evaluated by calculating the commutator of the density matrix and this Hamiltonian. The normalization factors have been omitted in these equations since they are not needed for a mere qualitative description. Likewise, only a minimal number of spins  $A$  will be considered that may give an observable signal on the  $S$  spins. In this work, it is sufficient to account for two-spin operators containing one  $A$  and one  $S$  spin. The  $A$  spins are assumed to have the same spatial coordinates as the  $S$  spin. These simplifications preclude a precise description of the evolution due to the DF, neither the correct magnitude nor the angular dependence can be predicted. Nevertheless, it allowed a good insight into the original experiment where a DIPSI-2 sequence was used to transfer the coherence between  $A$  and  $S$  spins, and even provided a close estimate of the ratio of transfers into different coherence orders (Pelupessy, 2022b).

The effects of RD may mask or dampen those of the DF since the timescale in which RD occurs can be more than an order of magnitude shorter. However, in the experiments shown in this work, the former are suppressed by de-phasing the  $A$  spins with a  $90^\circ$  followed by a PFG, which allows us to focus on effects of the DF.

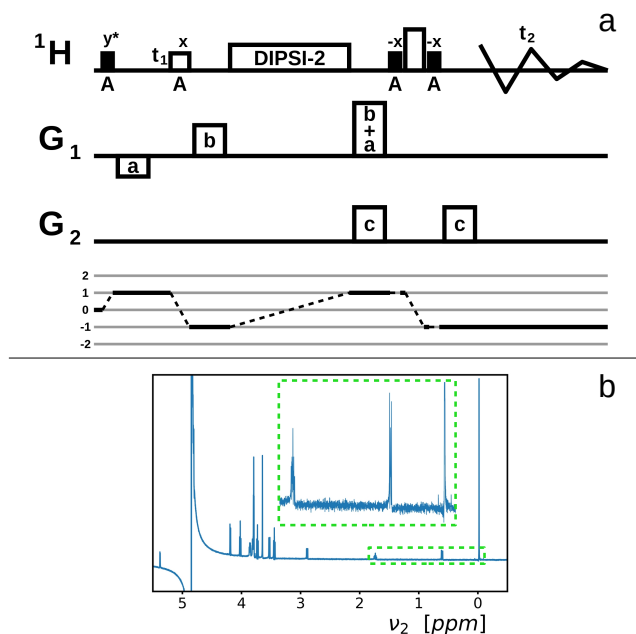


**Figure 2.** (a) Variant of the selective TOCSY pulse sequence that facilitates the transfer of phase coherence by the DF (Pelupessy, 2022b) adapted to record broadband in-phase spectra with high resolution in inhomogeneous fields and with solvent suppression. Filled and open rectangles stand for  $90^\circ$  and  $180^\circ$  rf pulses, respectively. Low amplitude pulses are selectively applied to the abundant  $A$  spins, as indicated by the characters  $A$  below the pulses, while the DIPSI-2 pulse-train and the high amplitude pulse are broadband. All pulses are applied along the  $x$  axis unless specified otherwise. The pulse marked with an asterisk is alternated in phase to achieve frequency discrimination in the indirect  $t_1$  dimension. Here, time-proportional phase increments (TPPI, Marion and Wuthrich (1983)) were used. The PFGs on the lines marked with  $G_1$ ,  $G_2$  and  $G_3$  ( $G_3$  is not used in this figure), are applied along three orthogonal axes. The coherence of the  $A$  spins is modulated by the two PFGs  $G_a$  and  $G_b$ . The amplitude of  $G_a$  must be large enough to quench effects of RD, but as low as possible to diminish losses due to diffusion. The area of  $G_{a+b}$  must be equal to the sum of the areas of  $G_a$  and  $G_b$ , the signs of the PFGs are indicated by positive or negative rectangles. In general, a PFG marked  $pa + qb$  means a PFG that is equal to the vector addition  $p$  times  $G_a$  and  $q$  times  $G_b$ . Purging PFGs  $G_c$  help to suppress the signal of the abundant  $A$  spins. The coherence selection pathway is plotted below the sequence. (b) 1D spectrum recorded with  $t_1 = 0$  and a DIPSI-2 irradiation time of 200 ms in a homogeneous  $B_0$  field.

### 3.1 High-resolution spectra in inhomogeneous fields

Fig. 2a depicts an adaptation of the selective TOCSY pulse sequence with DIPSI-2 rf irradiation used to transfer the phase coherence from the abundant solvent spins  $A$  to the solute spins  $S$ , that includes: 1) a Watergate spin-echo (Piotto et al., 1992) to obtain broadband in-phase spectra and solvent suppression, and 2) an indirect evolution period before the TOCSY pulse-train to record high-resolution spectra in inhomogeneous  $B_0$  fields in a manner similarly to experiments by Huang et al. (2010) that used the DF combined with spin-echo correlation spectroscopy (SECSY, Nagayama et al. (1979)). In fig. 2b, a 1D spectrum obtained with  $t_1 = 0$  in a homogeneous  $B_0$  field of 2 mM sucrose and 0.5 mM sodium 3-(trimethylsilyl)propane-1-sulfonate



(DSS) in a 90%/10% mixture of H<sub>2</sub>O/D<sub>2</sub>O (the same sample is used throughout this work). The inset, that shows part of the spectrum, highlights the small phase distortions at long DIPSI-2 irradiation times (> 100 ms), which cannot be simultaneously corrected for all resonances by a linear phase correction. The <sup>13</sup>C satellites on either side of the methyl protons correspond to a concentration of 22.5 μM.

The results of a 2D experiment in an inhomogeneous  $B_0$  field are shown in fig. 3a (the line-width at half height measured on the water resonance was about 225 Hz). The coherence selection pathway below the sequence in fig. 2 shows that  $B_0$  inhomogeneities that have evolved in  $t_1$  should be refocused in the course of the direct dimension at the time  $t_2 = t_1$ , which leads to the skewed line-shapes. In the indirect  $t_1$  dimension, the spectrum needs to cover the inhomogeneously broadened line-shape (here 1ppm was used). On the right (fig. 3b), a sliding window function has been applied in the direct  $t_2$  dimension and subsequently the spectrum has been sheared so that the elongated ridges appear perpendicular to the  $\nu_2$  axis. The window function consisted of zeroes for all time-points except for a narrow range of points  $k = \{-d + o, d + o\}$  where the intensities were multiplied by:

$$1 - \sin^{2n} \{ \pi * (k - bw_2 t_1) / (2d) \}, \quad (5)$$

where  $bw_2$  is the bandwidth in the direct dimension (the inverse of the time-increment), and the offset  $o$  is the integer nearest to  $bw_2 t_1$ . This function is identical to the amplitude modulation of wide-band, uniform rate and smooth truncation pulses (WURST, Kupce and Freeman (1995)). The higher the integer value  $n$ , the closer it is to a rectangular profile. The broader the inhomogeneous line, the sharper the echo and, consequently, the smaller the range  $2d$ . The variables  $d = 300$  and  $n = 1$  were empirically optimized (the value of  $n$  only slightly affects the result). The 1D spectrum in fig. 3c corresponds to the sum of the middle 112 rows (of a total of 512) of the latter 2D spectrum. The lower rows in figs. 3d and 3e show enlargements of this spectrum, the top rows show the regions of the spectrum of the first increment ( $t_1 = 0$ ) and the middle rows are the same regions, in a homogeneous  $B_0$  field, of a pulse-acquire experiment preceded by saturation of the solvent signal.

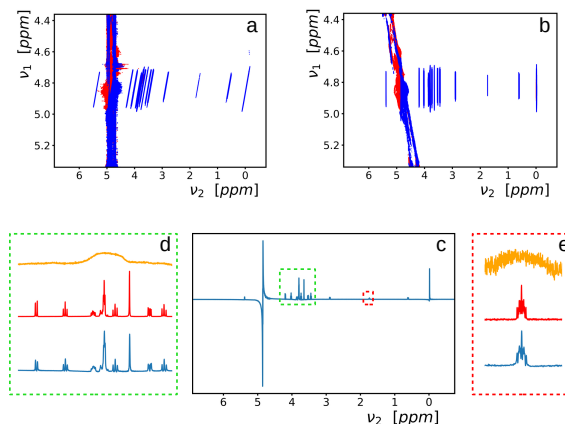


**Figure 3.** (a) 2D spectrum recorded with the pulse sequence of fig. 2a under the same conditions as the 1D spectrum of fig. 2b, except that the  $B_0$  field was purposely rendered inhomogeneous (line-widths of about 225 Hz). (b) The 2D spectrum of (a) has been tilted and a sliding window function (eq. 5) has been applied. (c) The sum of the central 112 rows of (b). (d, e) two regions of the spectrum have been enlarged on the bottom of these frames. In the center, plotted in red, the corresponding regions of a pulse-acquire spectrum, preceded by saturation of the solvent signal, in a homogeneous  $B_0$  field. On top, plotted in orange, the Fourier transform of the first time increment ( $t_1 = 0$ ) of the experiment.

### 125 3.2 Double quantum transfer

After the  $90^\circ$  pulse and the first gradient of the sequence in fig. 4a, the magnetization of both  $A$  and  $S$  spins <sup>S</sup> are <sup>are</sup> de-phased by PFG a. The commutator of the lowest order term, which contains a product of  $S$  and  $A$  spin operators in the expansion of the density operator, with  $H_{AS}^{eff}$  of eq. 4 results in:

$$-i[H_{AS}^{eff}, (c_a S_x + s_a S_y)(c_a A_x + s_a A_y)] = -(3/16)s_{2a}(S_z + A_z), \quad (6)$$

130 where  $c_a$  and  $s_a$  stand for  $\cos(\gamma\tau_a \mathbf{G}_a \cdot \mathbf{r})$  and  $\sin(\gamma\tau_a \mathbf{G}_a \cdot \mathbf{r})$ , with  $\tau_a$  the effective duration of  $\mathbf{G}_a$ . In general,  $c_{pa+qb}$  stands for  $\cos(\gamma\tau_a p \mathbf{G}_a \cdot \mathbf{r} + \gamma\tau_b q \mathbf{G}_b \cdot \mathbf{r})$ . Thus, the DIPSI-2 irradiation leads to a transfer of a DQ coherence involving the  $A$  and  $S$  spins to longitudinal magnetization. A purge gradient followed by a  $90^\circ$  rf pulse and another PFG in the same direction but with twice the area (with either the same or opposite sign) as  $\mathbf{G}_a$ , allows one to detect the longitudinal term of the sparse  $S$  spins. A possible phase difference  $\phi$  due to chemical shift evolution causes a phase shift  $\phi$  in the echo and additional longitudinal  
 135 components which are not modulated by the gradient.

In fig. 5a, the intensity,  $m_{xy} = \sqrt{m_x^2 + m_y^2}$ , of the methyl proton resonance of DSS is plotted as a function of the orientation angle  $\Theta_{G_a}$  of the PFG  $\mathbf{G}_a$  for a DIPSI-2 irradiation time of about 100 ms. The line that goes through the points corresponds to a function  $m_{xy}^0 (3 \cos^2 \Theta_{G_a} - 1)/2$ , where  $m_{xy}^0$  is the intensity recorded with the PFG oriented parallel to  $B_0$ . The line crosses zero at the so-called magic angle  $\Theta = 54.74^\circ$ . Although by definition all intensities are positive, for clarity, the intensities of  
 140 signals that point in opposite directions when phased identically are plotted with opposite signs.

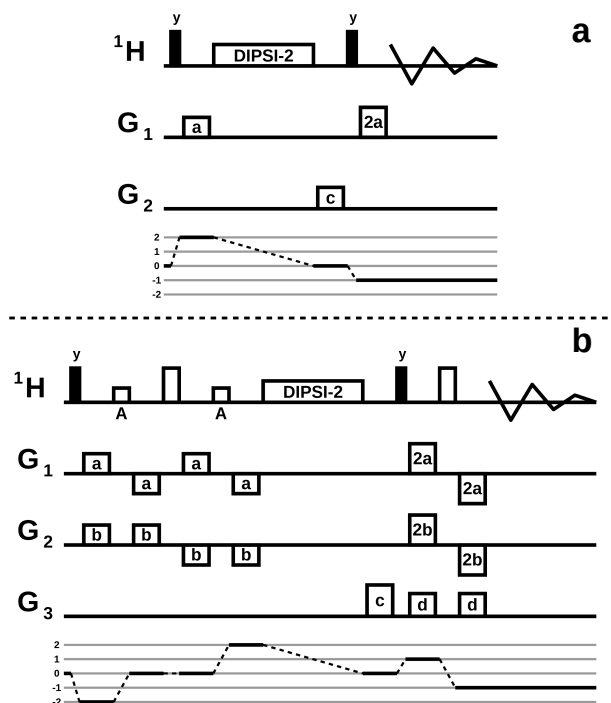


**Figure 4.** Pulse sequences where the DF mediates the transfer from a DQ coherence involving the abundant spins  $A$  and the sparse spins  $S$  to a longitudinal magnetization during the DIPSII-2 pulse-train. See the caption of fig. 2 for an explanation of the different rf pulses and PFGs. The coherence selection pathways are plotted below the sequences. (a) Non-selective experiment where both the solvent spins  $A$  and solute spins  $S$  are affected by  $G_a$ . After a purging PFG  $G_c$  and a  $90^\circ$  rf pulse, a PFG with twice the area of  $G_a$  is necessary to observe the signal of the  $S$  spins. (b) Same type of transfer as (a), with separate gradient labeling of spins  $A$  by  $4G_a$  and of spins  $S$  by  $4G_b$ . The signal of the  $S$  spins needs to be recovered by the sum of both PFGs. The two PFGs  $G_d$ , while not strictly necessary, improve the solvent suppression.

In fig. 5b, the buildup of intensities is plotted as a function of the irradiation time  $t_p$  for orientations parallel ( $\Theta_{G_a} = 0^\circ$ , blue squares) and perpendicular ( $\Theta_{G_a} = 90^\circ$ , blue circles) with respect to  $B_0$ . The blue dot-dashed lines are simulations of these experiments using the approximate solution of the non-linear Bloch eqs. 2 for the evolution of  $\mathbf{m}^A$ . The crosses in red are the intensities of the experiments of fig. 2 without any refocusing pulse, as described in Pelupessy (2022b) (for  $\Theta_G = 0^\circ$  and a coherence pathway selection  $+1 \rightarrow -1$ ). For clarity, the latter intensities have been divided by 2 since the (simplified) commutator formalism predicts that the initial slopes should differ by a factor 2.

In the sequence of fig. 4b, the solvent and solute spins are labeled by different gradients and the chemical shifts are refocused. The DF induces the following transfer:

$$-i \left[ H_{AS}^{eff}, (c_{4b}S_x - s_{4b}S_y)(c_{4a}A_x - s_{4a}A_y) \right] = (3/16)s_{4a+4b}S_z - (1/16)s_{4a-4b}S_z + \dots \quad (7)$$

The first term on the right can be recovered after a  $90^\circ$  pulse by the sum of the two PFGs,  $\pm(4G_a + 4G_b)$ . The solvent senses only  $G_a$  before the DIPSII-2 irradiation so that no additional measures need to be taken to suppress its signal after the DIPSII-2



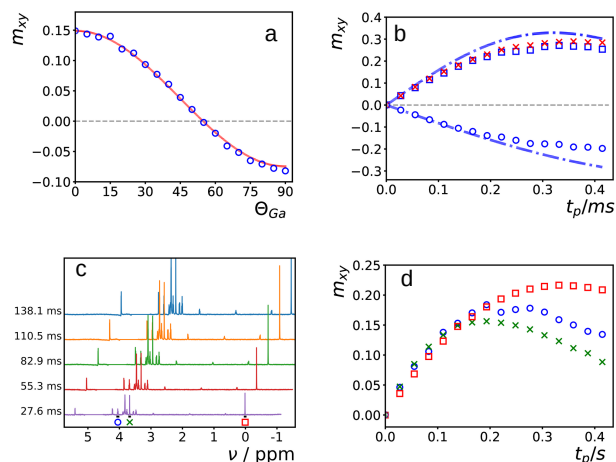


**Figure 5.** (a) Signal intensities of the methyl protons of DSS obtained with the sequence of fig. 4a with a DIPSI-2 irradiation time of 100 ms. The orientation of  $\mathbf{G}_a$  was varied while its amplitude was kept constant. While  $m_{xy}$  is always positive, it has been multiplied by  $-1$  for signals that were opposite with respect to the first one. The red line is a function proportional to  $3\cos^2\Theta_{G_a} - 1$  that goes through the first point. (b) At the angles  $\Theta_{G_a} = 0^\circ$  (blue squares) and  $\Theta_{G_a} = 90^\circ$  (blue circles) the evolution of the signal has been recorded as a function of DIPSI-2 irradiation time  $t_p$ . The dash-dotted lines are simulations as explained in main the text (without taking into account relaxation or translational diffusion). The red crosses are intensities, scaled down by a factor 2, obtained with the experiment described by Pelupessy (2022b). (c) Spectra of a solution of 2 mM sucrose and 0.5 mM DSS in  $\text{H}_2\text{O}/\text{D}_2\text{O}$  (90%/10%) recorded with the experiment of fig. 4b for several irradiation times  $t_p$  indicated on the left side of the spectra. The baseline of each spectrum has been corrected separately for the regions to the left and right of the solvent signal that has been digitally removed for clarity. (d) The buildup curves of three selected resonances marked at the bottom of (c).

irradiation and, consequently, the echo before signal detection can be shorter than the one in fig. 2. The amplitude  $\omega_D$  of the DF depends only on the orientation of  $\mathbf{G}_a$ .

In fig. 5c, spectra obtained with  $\mathbf{G}_a$  along the  $z$ -axis and  $\mathbf{G}_b$  along the  $x$ -axis for several DIPSI-2 times are displayed. The buildup curves of three resonances (the methyl resonance of DSS, and two sucrose resonances) are plotted in fig. 5d. The buildup curves are very similar at short times and start to diverge at longer times, probably due to differences in relaxation rates.

### 3.3 Mixed modulations

In this section, several schemes are presented where the density operator is prepared in different ways and where the transfer from a  $+1$  to a  $-1$  coherence order is recorded. At the start of the sequence of figure 6a, a PFG  $\mathbf{G}_a$  sandwiched between two selective  $90^\circ$  pulses modulates the amplitude of the magnetization of the abundant  $A$  spins. It is followed by a purging PFG

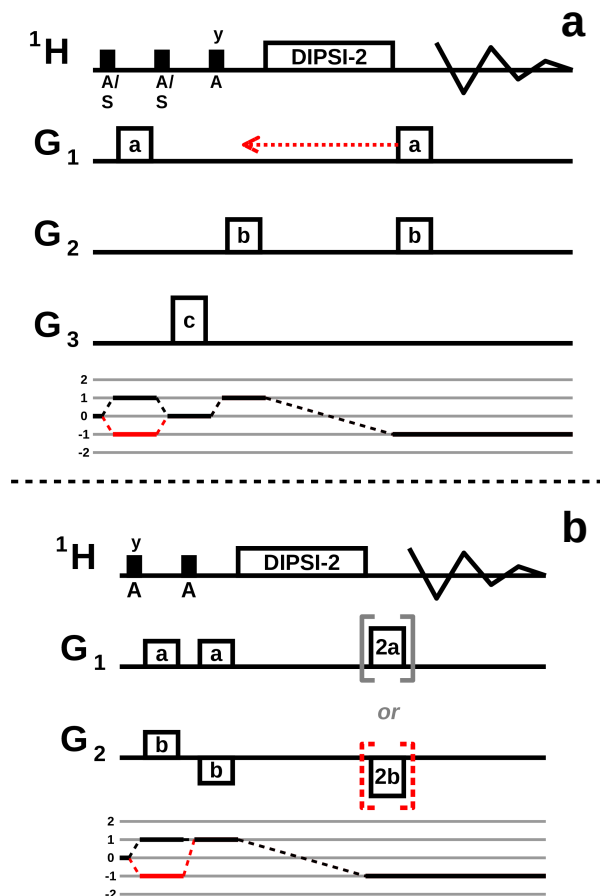


**Figure 6.** Variants of pulse sequences that record the transfer of phase coherence order from +1 to -1 by the DF. See the caption of fig. 2 for an explanation of the different rf pulses and PFGs. **(a)** A PFG  $G_a$  sandwiched between two selective  $90^\circ$  pulses modulates the amplitude of either the  $A$  or the  $S$  magnetization. After a purging PFG  $G_c$  and a  $90^\circ$  pulse  $G_b$  modulates the phase of the  $A$  spins. After the DIPSI-2 the newly created coherence on the  $S$  spins can be recovered by the two PFGs  $G_a$  and  $G_b$ . The gradient  $G_a$  which follows the DIPSI-2 pulse-train, can alternatively be put in front. In the latter case, the coherence order, shown in the diagram below the sequence, after the first rf pulse is -1 (marked in red in the coherence selection pathway diagram) instead of +1. **(b)** The combination of PFGs and rf pulses before the DIPSI-2 pulse-train create two DFs, due to a modulation of the magnetization of  $A$  in different directions, both of them mediating a transfer of phase coherence. Either the modulation due to  $G_a$  or the one due to  $G_b$  is recovered. When the gradient  $2G_a$  is used, the coherence order after the first rf pulse is +1, while for  $2G_b$  it is -1 (red line).

and another selective pulse and PFG  $G_b$  before DIPSI-2 irradiation. The transfer can be described as follows:  
occurring during the mixing

$$-i \left[ H_{AS}^{eff}, S_z (c_a c_b A_x + c_a s_b A_y) \right] = (2/16) c_a s_b S_x + (4/16) c_a c_b S_y + \dots \quad (8)$$



Using the relations  $c_a c_b = (c_{b+a} + c_{b-a})/2$  and  $c_a s_b = (s_{b+a} + s_{b-a})/2$ , the DF can be decomposed into two fields, one due  
 165 to the half of the magnetization of the  $A$  spins that is de-phased by  $\mathbf{G}_b - \mathbf{G}_a$  and the other due to the half that is de-phased by  
 $\mathbf{G}_b + \mathbf{G}_a$ . If the gradients  $\mathbf{G}_b$  and  $\mathbf{G}_a$  are oriented either parallel or perpendicular to  $B_0$ , both fields are characterized by same  
 amplitude  $\omega_D$ . With the first two pulses applied selectively to the  $S$  instead of to the  $A$  spins, the operator analysis remains  
 the same. Both experiments were performed with  $\mathbf{G}_b$  along  $z$  and  $\mathbf{G}_a$  along  $x$  and a DIPSI-2 irradiation time of 100 ms. The  
 areas of the PFGs have been varied to change the angle  $\Theta_{G_a+G_b}$  of the vector addition of  $\mathbf{G}_a$  and  $\mathbf{G}_b$  with respect to  $B_0$  while  
 170 keeping the amplitude constant. The transfer efficiency is plotted as a function of  $\Theta_{G_a+G_b}$  in figs. 7a and 7b for experiments  
 with the first two selective pulses applied to  $H_2O$  (spins  $A$ ) and applied to the methyl protons of DSS (spins  $S$ ), respectively.  
 Only in the experiments where all selective pulses are applied to  $H_2O$  the typical  $(3 \cos^2 \Theta - 1)$  dependence is observed. The  
 direction of the spatial modulation of the  $A$  spins is important, which does not change with  $\Theta_{G_a+G_b}$  in the experiments where  
 the first pulses are applied on the  $S$  spins. While for *intramolecular* two-spin operators it does not matter how an amplitude- or  
 175 phase-modulation has been created, for *intermolecular* two-spin operators eq. 8 does not provide the full picture. For a spin  $S$   
 at a given position, one has to consider the dipolar interactions with all spins  $A$  (Lee et al., 1996), whose spatial modulation is  
 different for the two experiments. The angular dependence is restored when the second gradient  $\mathbf{G}_a$  is put before the DIPSI-2  
 block instead of behind (red arrow in fig. 6a), as shown in fig. 7c.

For the experiment with all selective pulses on the abundant  $A$  spins of  $H_2O$ , the transfer is measured (fig. 7d) as a function of  
 180 DIPSI-2 irradiation time at angles  $\Theta_{G_a+G_b} = 15^\circ$  (blue circles) and  $\Theta_{G_a+G_b} = 80^\circ$  (green triangles). The dashed dotted curves  
 are simulations assuming the amplitude  $\omega_D$  is constant throughout the irradiation time, which may not entirely be correct since  
 the spatial pattern of the modulations of the magnetization of  $A$  will change in time (although the modulations will remain in  
 the plane spanned by the vectors in the directions of  $\mathbf{G}_b - \mathbf{G}_a$  and  $\mathbf{G}_b + \mathbf{G}_a$ ). The red crosses correspond to a experiment with  
 the first two selective pulses on DSS, the second gradient  $\mathbf{G}_a$  shifted before the DIPSI-2 block and  $\Theta_{G_a+G_b} = 15^\circ$ . The buildup  
 185 is almost undistinguishable from the one in blue circles. The simulated curves for the latter experiment (here the assumption of  
 a constant  $\omega_D$  is correct since the magnetization of  $A$  is modulated in one dimension only) are almost identical to the previous  
 ones, indicating that the approximation (a constant  $\omega_D$ ) used for the set of experiments with all selective pulses on  $H_2O$  is  
 reasonable for these DIPSI-2 irradiation times.

In the experiment above, the modulation of the magnetization could be decomposed into two directions that are not neces-  
 190 sarily orthogonal, each at the same angle with respect to  $B_0$ . Before the DIPSI-2 irradiation in the experiment in fig. 6b, the  
 density matrix includes intermolecular two-spin operators involving the  $S$  spins of the following form:

$$S_z \{ A_x c_{a+b} c_{a-b} + A_y c_{a+b} s_{a-b} \} = S_z \{ A_x (c_{2a} + c_{2b})/2 + A_y (s_{2a} - s_{2b})/2 \}. \quad (9)$$

A term containing  $S_z A_z$  (created by the second selective pulse) has been left out since it commutes with the effective dipolar  
 Hamiltonian of eq. 4, and thus will not lead to any observable signal. Eq. 9 corresponds to a situation where half of the  
 195 magnetization is modulated in the direction of  $\mathbf{G}_a$  the other half in the direction of  $\mathbf{G}_b$ . Experiments were performed with  
 $\mathbf{G}_a$  parallel and  $\mathbf{G}_b$  perpendicular to  $B_0$ , with different irradiation times. The blue circles in fig. 8 correspond to the signal  
 intensities of the methyl protons of DSS while using a PFG  $2\mathbf{G}_a$  before detection. The green squares were recorded using

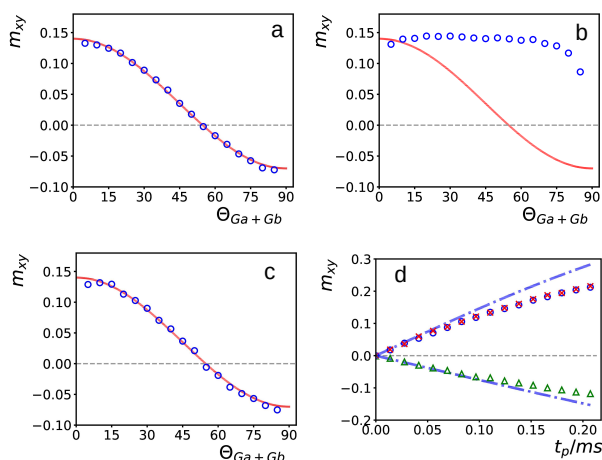


**Figure 7.** Signal intensities of the methyl protons of DSS obtained with the experiments of fig. 6a. **(a)** All selective pulses are applied on the solvent resonance. A DIPSI-2 irradiation time of 100 ms second has been used. The angle  $\Theta_{G_a+G_b}$ , i.e. the angle between the vector addition of PFGs  $G_a$  and  $G_b$  and  $B_0$  has been varied between  $5^\circ$  and  $85^\circ$ , while keeping the amplitude constant. **(b)** Same as (a), except that the first two  $90^\circ$  pulses are selectively applied on the methyl resonance. **(c)** same as (b), except that the PFG  $G_a$  which was placed just before acquisition has been moved in front of the DIPSI-2 pulse-train. The red lines in (a-c) correspond to a function  $0.14 \times (3 \cos^2 \Theta_{G_a+G_b} - 1)/2$ . **(d)** Signal intensities as a function of DIPSI-2 irradiation time  $t_p$ , recorded under the same conditions as in (a) with  $\Theta_{G_a+G_b} = 15^\circ$  (bleu circles) and  $80^\circ$  (green triangles) and as in (c) with  $\Theta_{G_a+G_b} = 15^\circ$ . The dash dotted curves are simulations as explained in the main text.

data corresponding to  
 a PFG  $-2G_b$ . The red crosses were recorded under the same circumstances as the second set experiments (i.e., with  $-2G_b$   
 before acquisition), except that  $G_a$  was perpendicular to  $G_b$  and  $B_0$ . The intensities of the latter experiments at longer times  
 200 are slightly higher than the intensities of the green squares. This is likely due to the larger perturbation of the longitudinal  
 magnetization of the  $S$  nuclei when one of the modulations is parallel to the  $B_0$  field. When the magnetization is modulated in  
 only one dimension the strength of the DF scales with the local value of  $m_A$ . This is not true anymore with the scheme describe  
 in this paragraph, since it can be decomposed into two different contributions each with its own amplitude. Remarkably, for a  
 given position in the sample the magnetization of the solute  $m_S$  may be affected by the DF even if the solvent magnetization  
 205 vanishes ( $m_A = 0$ ) at that position. Another counterintuitive feature is that even if the vector addition of the PFGs after the  
 first rf pulse and the vector addition of the PFGs after the second rf pulse point along the magic angle with respect to  $B_0$ , it  
 is still possible to observe a transfer of phase coherence.

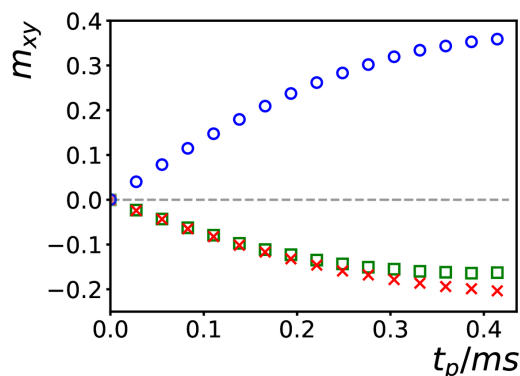


**Figure 8.** Buildup of the intensities of the methyl protons of DSS obtained with the experiment of fig. 6b at different DIPSI-2 irradiation times  $t_p$ .  $\mathbf{G}_a$  was parallel to  $B_0$ ,  $\mathbf{G}_b$  perpendicular. The blue circles were recorded using, just before acquisition,  $2\mathbf{G}_a$ , the green squares using  $-2\mathbf{G}_b$ . The red crosses have been recorded under the same conditions as the green squares, except that orientation of  $\mathbf{G}_a$  was perpendicular to  $B_0$  and  $\mathbf{G}_b$ .

#### 4 Experimental parameters

All experiments were acquired in a  $B_0$  field of 18.8 T (800 MHz proton frequency) at 290 K, with a probe equipped with coils  
210 to generate PFGs along three orthogonal axes. The rf amplitude  $\nu_1$  during the DIPSI-2 pulse-train was 8.33 kHz. The selective  
pulses on either the solvent or the methyl protons of DSS had Gaussian shapes and a length of 5 ms (for both the  $90^\circ$  and  
180° pulses), except the two  $90^\circ$  pulses in the Watergate scheme of fig. 2 which had a Sinc profile and a duration of 2 ms.  
The shaped pulses that were applied on the equilibrium magnetization of the abundant spins  $A$  were calibrated separately to  
correct for effects of RD. The PFGs had smoothed square profiles and a duration of 1 ms.  $G_1$ ,  $G_2$  and  $G_3$  indicate orthogonal  
215 gradient channels. The amplitudes of the PFGs were  $G_a = 1.6$  G/cm,  $G_b = 6.2$  G/cm,  $G_{a+b} = 7.8$  G/cm and  $G_c = 32$  G/cm for  
the experiments of figs. 2 and 3,  $G_a = 7.8$  G/cm,  $G_c = 27$  G/cm for figs. 5a and 5b,  $G_a = 1.95$  G/cm,  $G_b = 1.95$  G/cm,  $G_c = 27$   
G/cm and  $G_d = 10$  G/cm for figs. 5c and 5d,  $\|\mathbf{G}_a + \mathbf{G}_b\| = 7.8$  G/cm and  $G_c = 32$  G/cm for fig. 7,  $G_a = 3.9$  G/cm and  $G_b = 3.9$   
G/cm for fig. 8. For all experiments, 8192 complex points were acquired with a bandwidth of 12 ppm. The 2D spectrum of fig.  
3 has been acquired with 256 complex points, a bandwidth of 1 ppm and 4 scans per increment in the indirect dimension and a  
220 repetition time of 11 s (in the supporting information, results of a similar experiment recorded with only 1 scan and a repetition  
time of 3 s are shown to give an acceptable signal-to-noise ratio). The signal intensities have been normalized to either the  
spectrum of the methyl protons after a selective excitation or a broadband pulse-acquire experiment preceded by saturation of  
the solvent signal.



## 5 Conclusions

225 The dipolar field can cause an efficient intermolecular transfer of phase coherence rf irradiation sequences such as DIPSI-2 that  
 have been developed for total correlation spectroscopy. Since the transverse parts of the dipolar Hamiltonian are effective, the  
 DF can induce changes in coherence order. Experiments that result in broadband in-phase high-resolution spectra in inhomogeneous  
 fields have been designed. By combining several pulsed field gradients and rf pulses the DF may be tailored in such  
 a manner that it can be decomposed into different components that have their own spatial modulation and, hence, can bring  
 230 about different transfer processes.

### Appendix A: Evolution of the magnetization under continuous on-resonance irradiation

Consider the case of a constant on-resonance rf field. Without loss of generality, the rf field can be oriented along the  $x$ -axis.  
 Hence, for the abundant  $A$  spins, the set of equations 2 can be written as:

$$\begin{aligned}\dot{m}_x^A &= -2\alpha m_z^A m_y^A, \\ \dot{m}_y^A &= (2\alpha m_x^A - \omega_{1x}) m_z^A, \\ \dot{m}_z^A &= \omega_{1x} m_y^A,\end{aligned}\tag{A1}$$

235 where  $\alpha = 3\omega_D/4$ . In terms of:

$$\begin{aligned}m_+^A &= m_y^A + im_z^A, \\ m_-^A &= m_y^A - im_z^A,\end{aligned}\tag{A2}$$

eqs. A1 become:

$$\begin{aligned}\dot{m}_x^A &= i\alpha(m_+^A m_+^A - m_-^A m_-^A)/2, \\ \dot{m}_+^A &= i\alpha m_x^A m_-^A + i(\omega_{1x} - \alpha m_x^A) m_+^A, \\ \dot{m}_-^A &= -i\alpha m_x^A m_+^A - i(\omega_{1x} - \alpha m_x^A) m_-^A,\end{aligned}\tag{A3}$$

Usually,  $m_+$  and  $m_-$  are defined in terms of transverse operators. This traditional definition could have been kept by trans-  
 240 forming to a tilted frame. Switching to a rotating frame around the  $x$ -axis:

$$\begin{aligned}m_+^{\prime A} = e^{-i\omega_{1x}t} m_+^A &\implies m_+^A = e^{i\omega_{1x}t} m_+^{\prime A}, \\ m_-^{\prime A} = e^{i\omega_{1x}t} m_-^A &\implies m_-^A = e^{-i\omega_{1x}t} m_-^{\prime A},\end{aligned}\tag{A4}$$

one obtains:

$$\begin{aligned}\dot{m}_x^A &= i\alpha(e^{2i\omega_{1x}t} m_+^{\prime A} m_+^{\prime A} - e^{-2i\omega_{1x}t} m_-^{\prime A} m_-^{\prime A})/2, \\ \dot{m}_+^{\prime A} &= i\alpha e^{-2i\omega_{1x}t} m_x^A m_-^{\prime A} - i\alpha m_x^A m_+^{\prime A}, \\ \dot{m}_-^{\prime A} &= -i\alpha e^{2i\omega_{1x}t} m_x^A m_+^{\prime A} + i\alpha m_x^A m_-^{\prime A}.\end{aligned}\tag{A5}$$



When the oscillating components can be neglected (i.e., when  $|\omega_{1x}| \gg |\alpha|$ ), the solution is a nutation around the  $x$ -axis with  
245 an angular frequency of  $\alpha m_x^A(0)$  and hence in the original frame this results in:

$$\begin{aligned} m_x^A &= m_x(0) \\ m_y^A &= \cos\{\omega_{1x}t - \alpha m_x^A(0)t\} m_y^A(0) - \sin\{\omega_{1x}t - \alpha m_x^A(0)t\} m_z^A(0), \\ m_z^A &= \cos\{\omega_{1x}t - \alpha m_x^A(0)t\} m_z^A(0) + \sin\{\omega_{1x}t - \alpha m_x^A(0)t\} m_y^A(0). \end{aligned} \tag{A6}$$

*Competing interests.* The author has no conflicts of interest to declare.

250 *Acknowledgements.* I thank Geoffrey Bodenhausen for careful reading and correcting the manuscript.



## References

- Bernier, M. and Delrieu, J.: Measurement of Susceptibility of Solid He-3 Along Melting Curve from 20 Mk down to Nuclear Ordering Temperature, *Phys. Lett. A*, 60, 156–158, [https://doi.org/10.1016/0375-9601\(77\)90414-5](https://doi.org/10.1016/0375-9601(77)90414-5), 1977.
- Bloembergen, N. and Pound, R.: Radiation Damping in Magnetic Resonance Experiments, *Phys. Rev.*, 95, 8–12, <https://doi.org/10.1103/PhysRev.95.8>, 1954.
- 255 Bloom, S.: Effects of Radiation Damping on Spin Dynamics, *J. Appl. Phys.*, 28, 800–805, <https://doi.org/10.1063/1.1722859>, 1957.
- Bowtell, R., Bowley, R., and Glover, P.: Multiple Spin Echoes in Liquids in a High Magnetic-Field, *J. Magn. Reson.*, 88, 643–651, [https://doi.org/10.1016/0022-2364\(90\)90297-M](https://doi.org/10.1016/0022-2364(90)90297-M), 1990.
- Deville, G., Bernier, M., and Delrieux, J.: Nmr Multiple Echoes Observed in Solid He-3, *Phys. Rev. B*, 19, 5666–5688, <https://doi.org/10.1103/PhysRevB.19.5666>, 1979.
- 260 Dickinson, W.: The Time Average Magnetic Field at the Nucleus in Nuclear Magnetic Resonance Experiments, *Phys. Rev.*, 81, 717–731, <https://doi.org/10.1103/PhysRev.81.717>, 1951.
- Edzes, H.: The Nuclear Magnetization as the Origin of Transient Changes in the Magnetic-Field in Pulsed Nmr Experiments, *J. Magn. Reson.*, 86, 293–303, [https://doi.org/10.1016/0022-2364\(90\)90261-7](https://doi.org/10.1016/0022-2364(90)90261-7), 1990.
- 265 Enns, T., Ahn, S., and Warren, W. S.: Visualizing the dipolar field in solution NMR and MR imaging: three-dimensional structure simulations, *Chem. Phys. Lett.*, 305, 101–108, [https://doi.org/10.1016/S0009-2614\(99\)00366-8](https://doi.org/10.1016/S0009-2614(99)00366-8), 1999.
- He, Q., Richter, W., Vathyam, S., and Warren, W.: Intermolecular Multiple-Quantum Coherences and Cross Correlations in Solution Nuclear-Magnetic-Resonance, *J. Chem. Phys.*, 98, 6779–6800, <https://doi.org/10.1063/1.464770>, 1993.
- Huang, Y., Cai, S., Chen, X., and Chen, Z.: Intermolecular single-quantum coherence sequences for high-resolution NMR spectra in inhomogeneous fields, *J. Magn. Reson.*, 203, 100–107, <https://doi.org/10.1016/j.jmr.2009.12.007>, 2010.
- 270 Kramer, F., Peti, W., Griesinger, C., and Glaser, S. J.: Optimized homonuclear Carr-Purcell-type dipolar mixing sequences, *J. Magn. Reson.*, 149, 58–66, <https://doi.org/10.1006/jmre.2000.2271>, 2001.
- Kupce, E. and Freeman, R.: Adiabatic pulses for wide-band inversion and broad-band decoupling, *J. Magn. Reson. A*, 115, 273–276, <https://doi.org/10.1006/jmra.1995.1179>, 1995.
- 275 Lee, S., Richter, W., Vathyam, S., and Warren, W. S.: Quantum treatment of the effects of dipole-dipole interactions in liquid nuclear magnetic resonance, *J. Chem. Phys.*, 105, 874–900, <https://doi.org/10.1063/1.471968>, 1996.
- Lin, Y., Huang, Y., Cai, S., and Chen, Z.: Intermolecular Zero Quantum Coherence in NMR Spectroscopy, in: *Annual Reports on Nmr Spectroscopy*, Vol 78, edited by Webb, G. A., vol. 78, pp. 209–257, Elsevier Academic Press Inc, San Diego, <https://doi.org/10.1016/B978-0-12-404716-7.00005-5>, 2013.
- 280 Marion, D. and Wuthrich, K.: Application of Phase Sensitive Two-Dimensional Correlated Spectroscopy (cosy) for Measurements of H-1-H-1 Spin-Spin Coupling-Constants in Proteins, *Biochem. Biophys. Res. Commun.*, 113, 967–974, [https://doi.org/10.1016/0006-291X\(83\)91093-8](https://doi.org/10.1016/0006-291X(83)91093-8), 1983.
- Nagayama, K., Wuthrich, K., and Ernst, R.: 2-Dimensional spin-echo correlated spectroscopy (SCSY) for H-1-NMR studies of biological macromolecules, *Biochem. Biophys. Res. Commun.*, 90, 305–311, [https://doi.org/10.1016/0006-291X\(79\)91625-5](https://doi.org/10.1016/0006-291X(79)91625-5), 1979.
- 285 Pelupessy, P.: Radiation damping strongly perturbs remote resonances in the presence of homonuclear mixing, *Magnetic Resonance*, 3, 43–51, <https://doi.org/10.5194/mr-3-43-2022>, 2022a.





- Pelupessy, P.: Transfer of phase coherence by the dipolar field in total correlation liquid state nuclear magnetic resonance spectroscopy, *J. Chem. Phys.*, 157, 164–202, <https://doi.org/10.1063/5.0120909>, 2022b.
- Piotto, M., Saudek, V., and Sklenar, V.: Gradient-Tailored Excitation for Single-Quantum Nmr-Spectroscopy of Aqueous-Solutions, *J. Biomol. NMR*, 2, 661–665, <https://doi.org/10.1007/BF02192855>, 1992.
- 290 Rucker, S. and Shaka, A.: Broad-Band Homonuclear Cross Polarization in 2d Nmr Using Dipsi-2, *Mol. Phys.*, 68, 509–517, <https://doi.org/10.1080/00268978900102331>, 1989.
- Shaka, A., Keeler, J., and Freeman, R.: Evaluation of a New Broad-Band Decoupling Sequence - Waltz-16, *J. Magn. Reson.*, 53, 313–340, [https://doi.org/10.1016/0022-2364\(83\)90035-5](https://doi.org/10.1016/0022-2364(83)90035-5), 1983.
- 295 Shaka, A., Barker, P., and Freeman, R.: Computer-Optimized Decoupling Scheme for Wideband Applications and Low-Level Operation, *J. Magn. Reson.*, 64, 547–552, [https://doi.org/10.1016/0022-2364\(85\)90122-2](https://doi.org/10.1016/0022-2364(85)90122-2), 1985.
- Suryan, G.: Nuclear Magnetic Resonance and the Effect of the Methods of Observation, *Curr. Sci.*, 18, 203–204, <https://www.jstor.org/stable/24212060>, 1949.
- Vathyam, S., Lee, S., and Warren, W. S.: Homogeneous NMR spectra in inhomogeneous fields, *Science*, 272, 92–96, <https://doi.org/10.1126/science.272.5258.92>, 1996.
- 300 Warren, W., Richter, W., Andreotti, A., and Farmer, B.: Generation of Impossible Cross-Peaks Between Bulk Water and Biomolecules in Solution Nmr, *Science*, 262, 2005–2009, <https://doi.org/10.1126/science.8266096>, 1993.
- Warren, W. S., Lee, S., Richter, W., and Vathyam, S.: Correcting the classical dipolar demagnetizing field in solution NMR, *Chem. Phys. Lett.*, 247, 207–214, [https://doi.org/10.1016/0009-2614\(95\)01184-5](https://doi.org/10.1016/0009-2614(95)01184-5), 1995.